

# Gravitational waves from colliding black holes

Chris Pedersen

May 3, 2017

## Abstract

A complete understanding of the LIGO detectors' ability to accurately measure spin parameters is of key importance to understanding the astrophysics of binary black hole systems. Of particular significance is an ability to determine spin orientations as a means of distinguishing between binary formation models. In this work we overview the core physics of gravitational waves, relativistic precession in binary systems, the LIGO detectors, and the techniques involved in parameter estimation. We then examine the specific effects of precession on a gravitational waveform. The technique of 'matching' between waveforms is used as a computationally cheap way to explore degeneracies in the parameter space. A series of signals are then injected into simulated detector noise, and a full parameter estimation is performed on the data segments. Using the match results as a guide, we target these injections to areas in the parameter space where we expect to be particularly sensitive and insensitive to spin parameters. Inference for a full range of inclinations and phases is performed, and we identify areas where spin orientations are consistently incorrectly recovered. We then briefly examine the impact the upcoming VIRGO detector will have on spin estimation.

## Contents

<b>1</b>	<b>Introduction</b>	<b>3</b>
1.1	A Brief History . . . . .	3
1.2	Gravitational waves and their sources . . . . .	4
1.3	LIGO . . . . .	7
1.4	Parameter estimation . . . . .	7
1.5	Precession and its astrophysical importance . . . . .	10
<b>2</b>	<b>Intrinsic degeneracies</b>	<b>13</b>
2.1	Precessing waveforms . . . . .	13
2.2	Matching and exploring the parameter space . . . . .	15
<b>3</b>	<b>Detector response simulations</b>	<b>18</b>
3.1	Signal extraction . . . . .	18
3.2	Inference pipeline . . . . .	18
3.3	Inference results . . . . .	18
3.4	Inclination and precession . . . . .	23
3.5	Impact of Virgo . . . . .	23
<b>4</b>	<b>Conclusions</b>	<b>23</b>



# 1 Introduction

## 1.1 A Brief History

The first[1] and subsequent[2] observations of gravitational waves (GWs) came around the centenary of Einstein’s theoretical prediction of their existence[3][4]. Einstein noticed that a solution to the linearised approximations of his field equations took the form of a wave equation[5], and that the source of these waves would be an asymmetric, massive, rotating system, such as a binary star system. As the amplitude of the waves was predicted to be so incredibly weak, with strain amplitudes on the order of  $10^{-24}$ , at the time there was no hope of ever actually detecting them, and Einstein even questioned whether they were physically real at all[6]. Observations of the Hulse-Taylor pulsar (PSR 1913+16)[7] showed that the energy loss of the binary agreed perfectly with the rate predicted by gravitational wave emission, providing indirect evidence of GWs and resulting in the award of the 1993 Nobel Prize in Physics, but it was not until the construction of the Laser-Interferometric Gravitational wave Observatory (LIGO) that direct detection of gravitational waves became possible - a truly remarkable feat of science and engineering involving the most precise measurements ever made by several orders of magnitude.

Now that the existence of gravitational waves has been confirmed and their detection is possible we enter a new era of astronomy, and it is difficult to overstate the wealth of science that is now attainable in the coming decades. Gravitational waves can be used to study astrophysical phenomena that cannot be observed using electromagnetic radiation, such as binary black hole (BBH) systems where two inspiralling black holes merge into one, as well as being used in conjunction with electromagnetic observations in ‘multi-messenger’ astronomy where events such as supernovae and gamma ray bursts are thought to release both gravitational and electromagnetic radiation which can be studied in conjunction with one another[8][9]. In addition GWs can be used to conduct the closest tests of general relativity (GR) to date[10][11] as well as to further inform the ongoing development of quantum gravity models[12]. Currently the LIGO network consists of two detectors, one in Hanford WA (H1), one in Livingston LA (L1), however there are three detectors that will be added to the network in the coming years, with VIRGO (V1) in Italy due to come online by the end of 2017, and with LIGO India and KAGRA joining later. In addition to this, there are also proposals underway for a space-based gravitational wave observatory, the Laster Interferometric Space Antenna (LISA)[13] which would be able to explore a different frequency-range and therefore study a range of different astrophysical objects to those observed using earth-based detectors.

This project focuses on studying the merging of a binary system, known as a compact binary coalescence (CBC). This term includes the merging of binary neutron star systems and neutron star-black hole systems, but in this work we focus on the merging of BBHs, where we do not consider the internal structure of the compact binary objects unlike in the case of systems involving neutron stars. We focus on parameter estimation of BBH mergers, with a specific emphasis on inferring the spin parameters of the component BHs in systems where the spins are misaligned, and how they can be determined through careful analysis of LIGO data.

The work is structured as follows; first we present an overview of gravitational wave theory and the LIGO detectors. We then discuss the process of parameter estimation and the mathematical and computational techniques that are used. Next we consider the case

of systems with misaligned spins where relativistic precession is manifested, and consider the specific set of challenges this raises for signal analysis and parameter estimation. The astrophysical significance of studying precessing systems is also discussed. In chapter 2 we introduce the concept of ‘matching’ as a method for quantifying the degeneracy between different waveforms with minimal computational effort, and use these matches to identify the parts of the parameter space that would be most fruitful to explore. In chapter 3 we describe the process of software injections, where simulated signals are inserted into detector noise and then recovered using the inference methods introduced in the introduction. This gives a way of probing the detector response to a given signal. We present results from a range of software injections guided by the match findings, and attempt to analyse how effectively the current infrastructure is capable of inferring spin parameters on precessing BBHs. Finally we briefly consider the impact of the upcoming VIRGO detector on spin inference. The majority of the computational tasks involved in this work are performed in the PyCBC environment[14], including the generation of waveforms, simulations of the detector response to gravitational waves, finding the matches between waveforms and running inference on data segments.

## 1.2 Gravitational waves and their sources

A complete analysis is available in Hartle[15], but here we briefly overview the fundamental theory of gravitational waves. In the general theory of relativity, gravity is a consequence of the curvature of a 4-dimensional spacetime as described by the Einstein equation (in natural units):

$$R_{\alpha\beta} - \frac{1}{2}g_{\alpha\beta}R = 8\pi T_{\alpha\beta} \quad (1)$$

where  $R_{\alpha\beta}$  is the Riemannian curvature tensor,  $g_{\alpha\beta}$  is the metric tensor,  $R$  is the Ricci scalar and  $T_{\alpha\beta}$  is the energy-momentum tensor. This equation is essentially ten non-linear partial differential equations, where we use the Einstein summation convention to sum over all indices, and where indices run from 0 to 4 and all tensors are symmetric. Intuitively, the LHS of this equation can be thought of as the local curvature of spacetime, and the RHS quantifies the energy and momentum density. In the weak-field regime, where the curvature of spacetime is low, the metric tensor can be approximated as

$$g_{\alpha\beta}(x) = \eta_{\alpha\beta} + h_{\alpha\beta}(x). \quad (2)$$

where  $\eta_{\alpha\beta}$  is the Minkowski metric and  $|h_{\alpha\beta}| \ll 1$  for all components. This metric can be substituted into the Einstein equation, and expanding in  $h_{\alpha\beta}$  in first order and using the Lorentz gauge, the Einstein equation becomes

$$\square h_{\alpha\beta} = 0 \quad (3)$$

where  $\square$  is the D’Alembertian operator, with the condition that

$$\partial_\beta h_\alpha^\beta - \frac{1}{2}\partial_\alpha h_\beta^\beta = 0. \quad (4)$$

The general solution to this equation is

$$h_{\alpha\beta} = \begin{pmatrix} 0 & 0 & 0 & 0 \\ 0 & a_+ & a_\times & 0 \\ 0 & a_\times & -a_+ & 0 \\ 0 & 0 & 0 & 0 \end{pmatrix} e^{i\omega(z-t)} \quad (5)$$

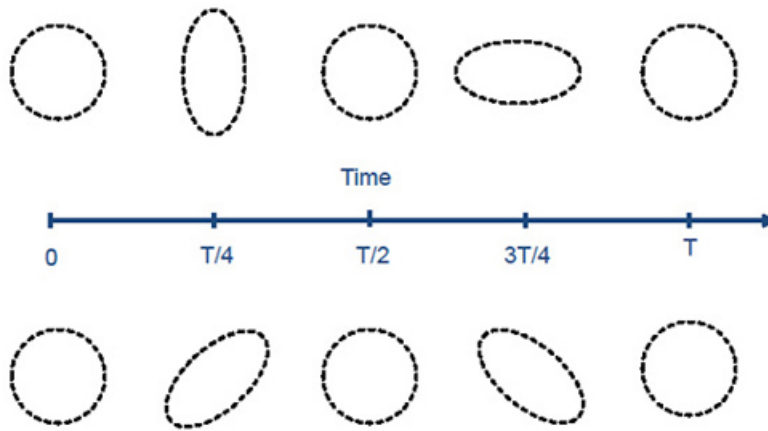


Figure 1: [16] Plus and cross polarisations respectively of a gravitational wave propagating through the page, with scale greatly exaggerated.

for a wave with frequency  $\omega$  propagating in the  $z$  direction. Here the  $a_+$  and  $a_\times$  terms represent the amplitudes of the 'plus' and 'cross' polarisations respectively. As a gravitational wave passes through an observer, spacetime is distorted along the spatial directions orthogonal to the propagation direction of the wave according to these polarisation amplitudes. A visualisation of this is shown in Fig. 1. It is this stretching and squeezing of spacetime that the LIGO detectors were built to detect.

Now we consider the sources of these waves. Analysis in this area can rapidly become extremely complicated as the weak-field approximation is dropped and higher orders of perturbations are included[17], but the simplest case is still instructive.

Approximating that the field around the source is still weak, that the wavelength is long and that the observer is a large distance from the source, the spatial elements of the GW metric are

$$h_{ij} \approx \frac{2}{r} \ddot{I}^{ij}(t - r) \quad (6)$$

where  $I^{ij}$  is the second mass moment given by

$$I^{ij}(t) = \int d^3x \mu(t, \vec{x}) x^i x^j \quad (7)$$

where  $\mu(t, \vec{x})$  is the mass density of the system. The energy loss of a binary system emitting gravitational waves is

$$L_{GW} = \frac{128}{5} M^2 R^4 \Omega^6, \quad (8)$$

and as the binary loses energy, the separation between the compact objects decreases, increasing the orbital frequency. Given the connection between the mass distribution of the system in (7) and the GW amplitudes in (6), this gives rise to a 'chirp' effect seen in the signal of a CBC GW. This is shown in a Fig. 3. which is a simulated waveform of the merging of a BBH system.

The waveform can be split into three phases - the inspiral, the merger and the ringdown. The frequency, frequency evolution and amplitudes of each polarisation of the GW emitted from a merger will depend on the properties of the system itself, and as such there is information about the source contained in the specific morphology of a GW signal.

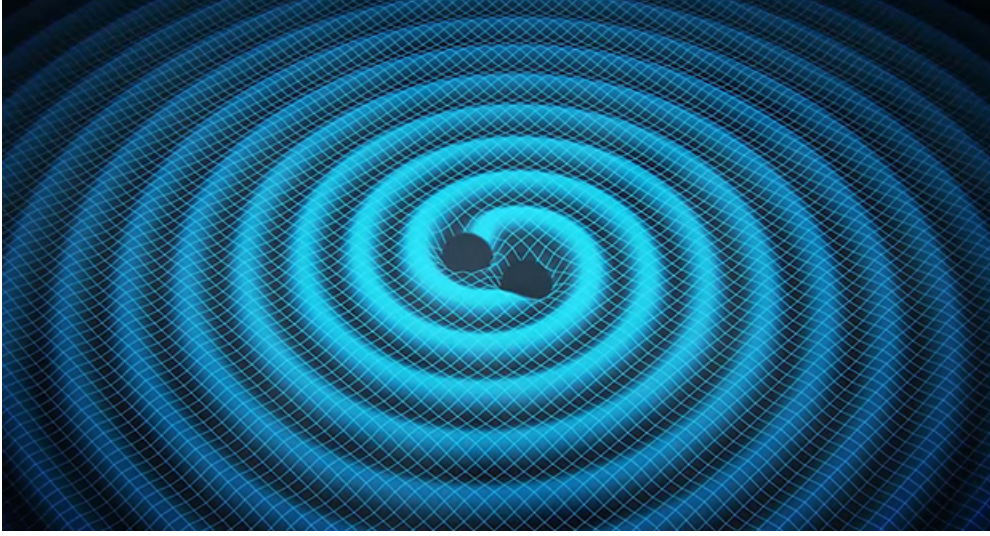


Figure 2: [18]Impression of two inspiralling compact objects emitting gravitational waves

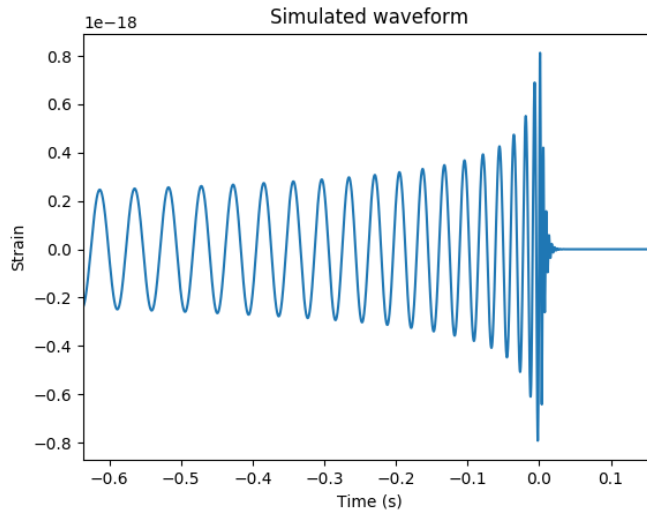


Figure 3: Simulated waveform of a BBH merger of two 35 solar mass black holes.

### 1.3 LIGO

The fundamental physical principle of the LIGO detectors is that they are laser interferometers. Interferometers are devices that can measure extremely small changes in length to high accuracy using constructive and destructive interference, as shown in Fig. 4. Light leaves the laser beam, and is split down the two arms of the detector by the beam splitter. If the length of the two arms is equal, the optical path difference between the two light beams is zero, and the two beams constructively interfere after recombining at the beam splitter. However if there is any change in the length of one of the arms, the beams will no longer constructively interfere and the photodetector will register a change in intensity. As a gravitational wave passes through the detector, the relative length of the arms changes, and the GW signal is recorded by the photodiode. A large part of the scientific and engineering effort at LIGO involves techniques to minimise and account for noise in the system, and the recent advanced LIGO upgrade to the detectors increased the effective volume within which mergers can be detected by an order of magnitude[21][22]. Some of these techniques include suspending the mirrors from a series of pulleys and penduli, and applying real time corrections to the positions of the mirrors to compensate for external seismic noise. There is also considerable effort in managing the optics and lasers of the system in order to maximise the coherence of the laser beam and the intensity detected in the photodiode[23]. The noise spectrum for advanced LIGO is shown in Fig. 5.[24], where the sharp noise peaks are specifically designed resonances that are removed from the strain data during signal processing. The strain data observed in the detector is a function of the different polarisation amplitudes

$$h(t) = F^+(\alpha, \delta, \psi)h_+(t) + F^\times(\alpha, \delta, \psi)h_\times(t), \quad (9)$$

where  $F^+(\alpha, \delta, \psi)$  and  $F^\times(\alpha, \delta, \psi)$  are the antenna beam patterns that describe how the detector responds to signals at different sky locations and polarisations[25]. In first order, the polarisations are given by

$$h_+(t) = A_{GW}(t)(1 + \cos^2(\iota) \cos(\phi(t))) \quad (10)$$

$$h_\times(t) = -2A_{GW}(t) \cos(\iota) \sin(\phi(t)) \quad (11)$$

and binaries that are face on (with  $\iota = 0$ ) emit circularly polarised waves, and edge-on binaries emit linearly (either cross or plus) polarised GWs. On completion of the advanced LIGO upgrade in 2015 the network had a detection band of 10-7000 Hz, allowing BBH mergers to be detected up to a redshift of  $z=0.4$ [23]. A variety of search algorithms continuously scan the data for a variety of signals[26][27] using tailored triggers and template banks depending on the kind of search being conducted. Once a candidate signal is identified, the data around the event is then separated, and a more targeted and computationally intensive parameter estimation analysis is performed on it.

### 1.4 Parameter estimation

A signal is described by a total of 16 parameters[28] - time and phase of coalescence  $t_c$  and  $\phi_c$ , two parameters to describe sky location (right ascension,  $\alpha$  and declination  $\delta$ ), luminosity distance  $D_L$ , inclination angle  $\iota$  describing the orientation of the binary's total angular momentum with respect to the line of sight, polarisation angle  $\psi$  which mixes plus

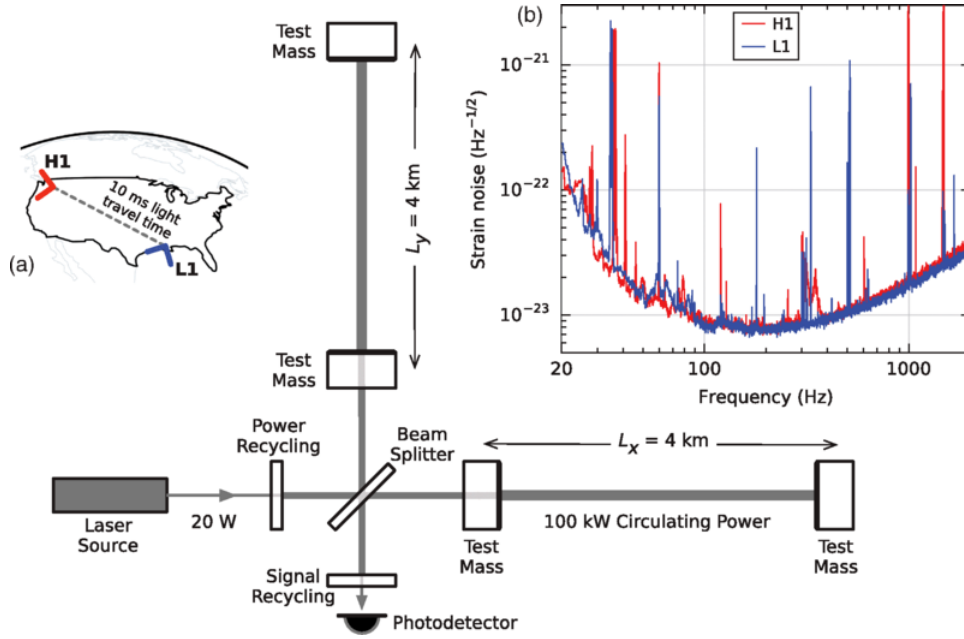


Figure 4: Simplified schematic of a LIGO detector[19] showing noise curves and detector location

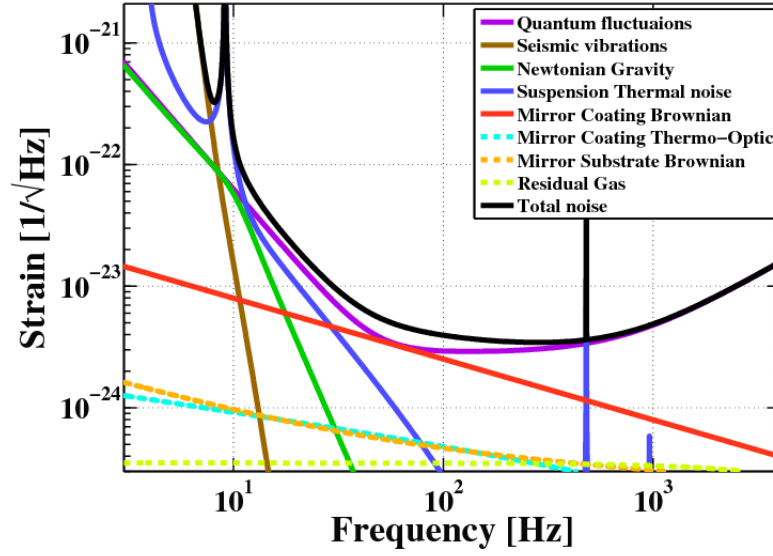


Figure 5: [20]Noise 'budget for advanced LIGO detectors.



and cross polarisations by  $h = h_+ \cos \psi + h_\times \sin \psi$ , the masses  $m_1, m_2$ , six spin parameters to totally describe the spins on each of the two black holes  $\vec{S}_1, \vec{S}_2$ , and then two eccentricity parameters. In this work we ignore the eccentricity parameters and consider only circular orbits for the sake of constraining the size of the already large parameter space, although the effect of these parameters is an area of active research. The masses and spins of the component black holes are intrinsic parameters which determine the morphology of the waveform, and the remaining are extrinsic parameters. The maximum spin a black hole can have is  $m^2$  in natural units, so the convention is to use a dimensionless spin magnitude  $a = |\vec{S}|/m^2 \leq 1$ . In the first order, the frequency evolution of the 'chirp' signal is approximated by a combination of the masses known as a the chirp mass

$$\mathcal{M} = \frac{(m_1 m_2)^{3/5}}{(m_1 + m_2)^{1/5}} \propto \left( f^{-11/3} \dot{f} \right)^{3/5} \quad (12)$$

so the specific morphology of the waveform is in some sense determined by a combination of the total mass and the mass ratio. We also define the total mass  $M = m_1 + m_2$ , and the mass ratio  $q = m_2/m_1$  adopting the convention that  $m_1 \geq m_2$ , so  $0 < q \leq 1$ . Given that so many parameters, many of them extrinsic, describe only two sets of timeseries data (one from each detector), parameter estimation is a challenging task and the parameter space is both enormous and wrought with degeneracies. Two of the more thoroughly researched degeneracies are those between total mass, distance and inclination, as all three parameters scale the amplitude of the signal and between mass and spin[29], which is a degeneracy that arises out of post-Newtonian (PN) theory.

The qualitative idea behind current methods of parameter estimation is that the GW signal is processed and extracted from the raw strain data, and then matched against an array of simulated waveforms to find which waveform most closely resembles the detected signal. The two technical challenges here are quantifying how well a template represents the observed signal, and how to efficiently sample the parameter space for new templates to test against the data. Within LIGO a standard method for quantifying the similarity between two signals  $h_1(t)$  and  $h_2(t)$  is given by the noise weighted inner product, also referred to as the 'match' between signals, and is defined as

$$\langle h_1(t) | h_2(t) \rangle = 2 \int_0^\infty \frac{\tilde{h}_1^*(f) \tilde{h}_2(f) + \tilde{h}_1(f) \tilde{h}_2^*(f)}{S_n(f)} df \quad (13)$$

where  $\tilde{h}(f)$  is the Fourier transform of the signal  $h(t)$ , and  $S_n(f)$  is the noise curve of the detector[30]. It is also convenient here to define the term *mismatch*, which is simply  $1 - m$  where  $m$  is the match. A variety of methods have been employed to sample the parameter space, including nested sampling[31] and analysis using Gaussian wavelets[28], and in this work we use a framework of Bayesian inference and Markov-Chain Monte Carlo methods[32][33][34]. This process results in a set of posterior distribution functions (PDFs) for each parameter. Using Bayes' Theorem, the posterior is given by

$$p(\vec{\theta} | d) = \frac{p(\vec{\theta}) p(d | \vec{\theta})}{P(d)} \quad (14)$$

where  $\vec{\theta}$  is an  $n$  dimensional vector in our parameter space of  $n$  parameters[31]. The first term in the numerator,  $p(\vec{\theta})$  is known as the *prior* distribution, and quantifies knowledge

we already have about the system that should influence our estimation of its' parameters. In practice, in inference of BBHs, the priors are almost always uniform or isotropic distributions. The denominator,  $P(d)$ , is essentially a normalisation factor ensuring that the posterior distribution integrates to unity. The crucial term is the *likelihood* for a given set of parameters given the data, which is determined by

$$p(d|\vec{\theta}) \propto \exp \left( -\frac{1}{2} \sum_{k=1,2} \left\langle h_k^M(\vec{\theta}) - d_k | h_k^M(\vec{\theta}) - d_k \right\rangle \right) \quad (15)$$

where the inner product is that defined in (13),  $d_k$  is the observed strain in the detector, and  $h_k^M(t; \vec{\theta})$  is the simulated detector response for a given set of parameters  $\vec{\theta}$  given by (9). The SNR is given by

$$\text{SNR} = \sqrt{\sum_{\text{det}} \int_{f_{\text{low}}}^{f_{\text{high}}} \frac{|h_{\text{det}}(f, \vec{\theta})|^2}{S_{\text{det}}(f)} df} \quad (16)$$

where the sum is over the detectors, and  $h_{\text{det}}(f, \vec{\theta})$  is the signal in the detector, and  $S_{\text{det}}(f)$  is the noise. The posterior distributions are sampled stochastically using a Markov-Chain Monte Carlo process and the Metropolis-Hasting algorithm. The qualitative idea behind this is that a sampler random walks across the parameter space. At each iteration, a random step in the parameter space is proposed, and the posterior is sampled at this new point. If the posterior has a higher value, this new point is used as the starting point for the next iteration. However if the posterior is lower, then the sampler only has a probability to jump to this new step proportional to the ratio of the posteriors at the current and proposed steps. In this way, after each iteration the distribution of samplers gets a step closer to accurately representing the posterior.

Various methods of waveform generation (known as *approximants*) have been employed, with varying degrees of computational intensity. In general, Post-Newtonian expansions are used in the inspiral phase where the gravitational field is weak enough for approximations to be sufficient. During the merger and ringdown, full numerical relativity simulations are required as the curvature is sufficiently strong that Post-Newtonian approximations are no longer valid[35][36]. These require significantly more computation time, and as such it is only in recent years that waveforms describing the full inspiral, merger and ringdown phases have become available.

## 1.5 Precession and its astrophysical importance

Considerable research has been done on studying non-spinning binaries and on non-precessing binaries where the spins are aligned or anti-aligned with the orbital angular momentum  $\vec{L}$ [37], but it is only recently that a more complete study of the parameter space has begun[38][39]. This is partly down to computational resources, as ignoring spin effects leads to a reduced parameter space and less computationally intensive waveforms. There are a unique set of challenges when considering binaries where the spins of the component black holes are not aligned  $\vec{L}$ , as due to relativistic effects, these binaries precess around the axis of total angular momentum  $\vec{J}$ , giving a time dependence to the orbital plane of the binary[40][41]. This causes the signal in the detector to have an overall amplitude

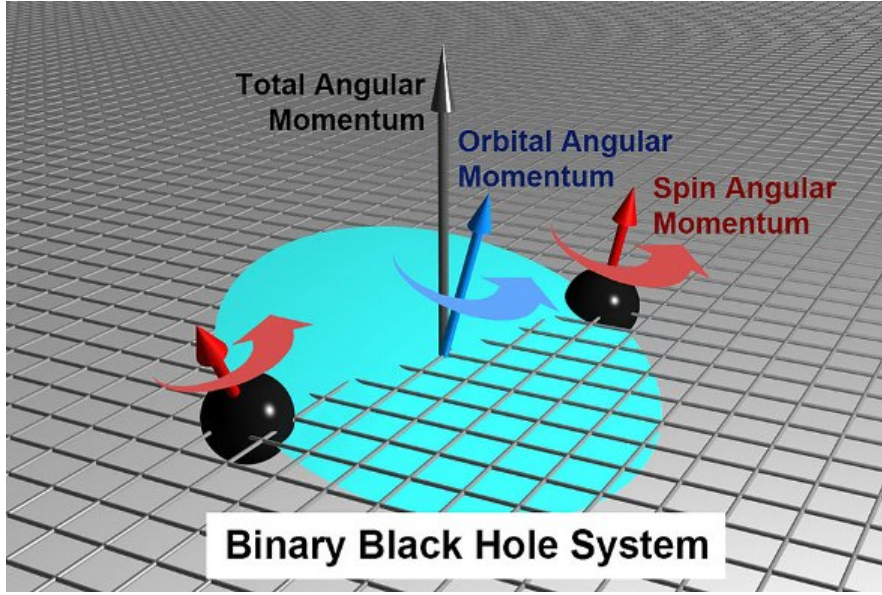


Figure 6: Illustration of a precessing binary system <https://phys.org/news/2015-03-insights-black-hole-collisions.html>

modulation as a function of time due to the change in orientation of the source, and therefore the change in direction of peak emission of GWs. This can be seen in Fig. 7, where we compare a very slightly precessing system with a maximally precessing one. Due to the computational intensity of dealing with both the generation of waveforms and inference process involving precessing systems, significant efforts have been made to reduce the size of the parameter space using the degeneracies between specific spin combinations to parametrise the spins of a binary. The most successful of these is the adoption of two spin parameters[36][42] that describe the whole binary system, where we replace the six spin parameters with two:

$$\chi_{\text{eff}} = \left( \frac{\mathbf{S}_1}{m_1} + \frac{\mathbf{S}_2}{m_2} \right) \cdot \frac{\hat{\mathbf{L}}}{M} \quad (17)$$

and

$$\chi_p = \frac{1}{B_1 m_1^2} \max(B_1 S_{1\perp}, B_2 S_{2\perp}) \quad (18)$$

where  $B_1 = 2 + 3/(2q)$  and  $B_2 = 2 + (3q)/2$ . These parameters effectively quantify the amount of in-plane and out of plane spin of the total binary, removing large degenerate portions of the parameter space. As different spin configurations within these parameters are effectively degenerate, no loss of information occurs in this re-parametrisation. The recent adoption of this parametrisation in the generation of template waveform banks (the IMRPhenomPv2 waveforms which, we use in this work) has made exploring the precessing parameter space computationally viable, as it reduces the computation time by an order of magnitude. The results of these waveforms agree well when compared with waveforms generated using the full spin parameter space (known as the Spinning Effective One Body Numerical Relativity, or SEOBNR waveforms)[43][44], so the recent availability of a computationally efficient precessing waveform bank makes this an opportune time to conduct this

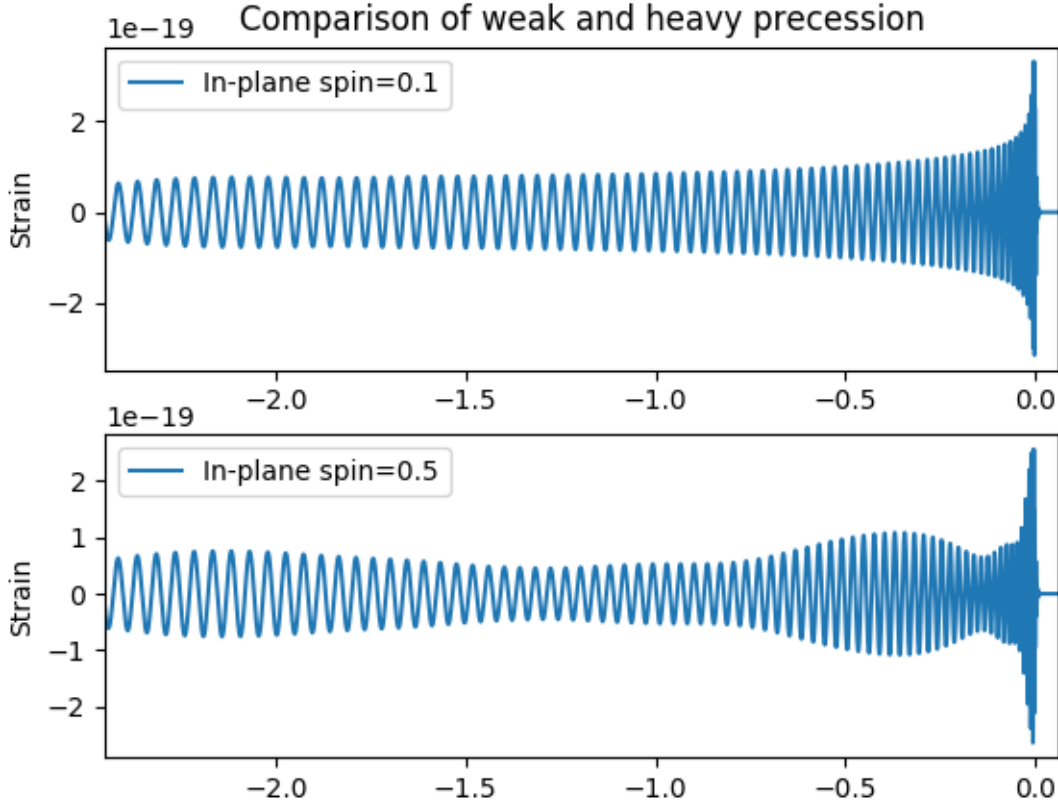


Figure 7: Waveforms for three BBH mergers with  $m_1 = 30$ ,  $m_2 = 10$  and with spins only in the  $x$  direction on the heavier black hole. The inclination is such that the binary is viewed edge-on. LEGEND ON THIS FIGURE IS WRONG, FIX BEFORE SUBMIT

research. Indeed the first full survey of an isotropic distribution of spins for a large number of simulations (200) has only very recently been published a matter of weeks ago[39].

The particular focus of this paper is on the challenges of inferring  $\chi_p$  in precessing systems. This parameter is of particular importance due to its astrophysical implications, and as of yet there has been no comprehensive study into the effects of precession and its amplitude modulation of the signal on the process of parameter estimation. The formation methods of compact binary systems of stellar mass black holes are currently unknown, and a variety of models have been proposed[45]. Of particular interest is whether the two black holes formed from a common accreting system, or whether the binary was formed by dynamical capture. The former model would imply that the spins on the black holes would generally tend to be aligned with one another and with the orbital angular momentum, however in the dynamical capture model we expect the spins to be more or less uniformly distributed. Given the large number of expected detections over the coming years, a thorough understanding of the detector's response to precessing waveforms and an accurate estimation of our ability to recover  $\chi_p$  reliably will be crucial to answering these questions, and maximising the scientific yield from this remarkable technology.

## 2 Intrinsic degeneracies

### 2.1 Precessing waveforms

We first consider in more detail the effects of precession on a GW waveform. This is important as understanding how precessive waveforms behave is key to understanding how the detector will respond to these signals, and understanding the detector response is the fundamental idea of parameter estimation. A closer look at equation (16), which essentially quantifies the amount of precession in a given binary, shows that it takes values in the range  $[0, 1]$ , with the maximum reached when the spin on the larger BH is fully in-plane. Even for a maximally precessing signal however, many possible configurations of polarisation and inclination are possible which will affect the way the amplitude of the signal is modulated. We show this in Fig. 8, where from this particular perspective the precessive effect appears largest in the case of the in-plane spin being 0.5, instead of the maximally precessing system with  $|\vec{S}| = 0.98$ . In this case, this is due to the fact that the inclination angle is defined with respect to the total angular momentum. In the case of precessing binaries,  $\vec{L}$  and  $\vec{J}$  are not aligned, so when we say we are viewing a binary 'edge-on', i.e. at  $\iota = \pi/2$ , the actual orbital plane of the system will not necessarily be edge-on. As a result, it is not always the case that precession affects are most noticeable in systems with the most precession, and a lot depends on the specific combination of source location and the polarisation and inclination angles for a specific event. The situation is further complicated by the fact that the phase,  $\phi_c$  is an important degree of freedom in precessing binaries, as shown in Fig. 9. In non-precessing binaries, the phase is very much a trivial parameter which contains no interesting information about the system, however in precessing binaries the phase has a significant affect on the signal modulation. This opens up the possibility of many different degeneracies between binaries with different intrinsic parameters but a certain combination of phase and source location, and makes studying precessing waveforms more challenging. When considering precession it is also important to note that heavier total mass binaries have considerably shorter inspiral phases, and therefore fewer oscillation cycles within the detection frequency band. So while they will

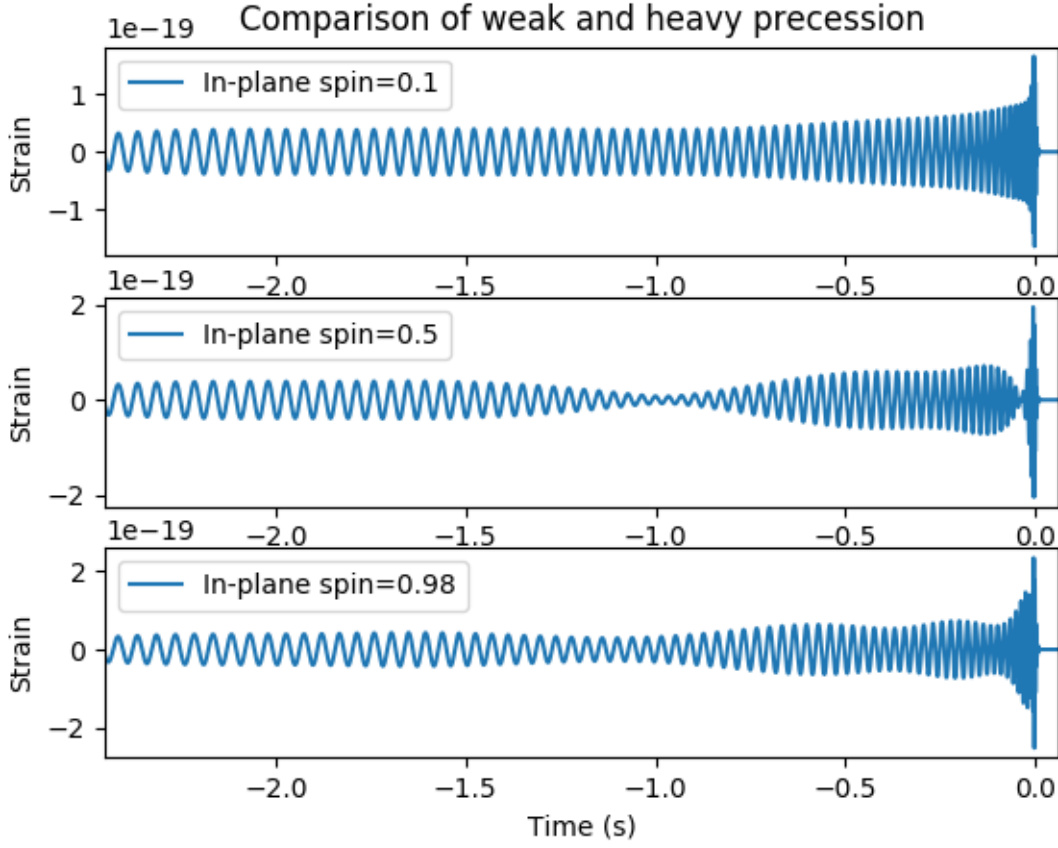


Figure 8: Waveforms for three BBH mergers with  $m_1 = 30$ ,  $m_2 = 10$  and with spins only in the  $x$  direction on the heavier black hole. The inclination is such that the binary is viewed edge-on.

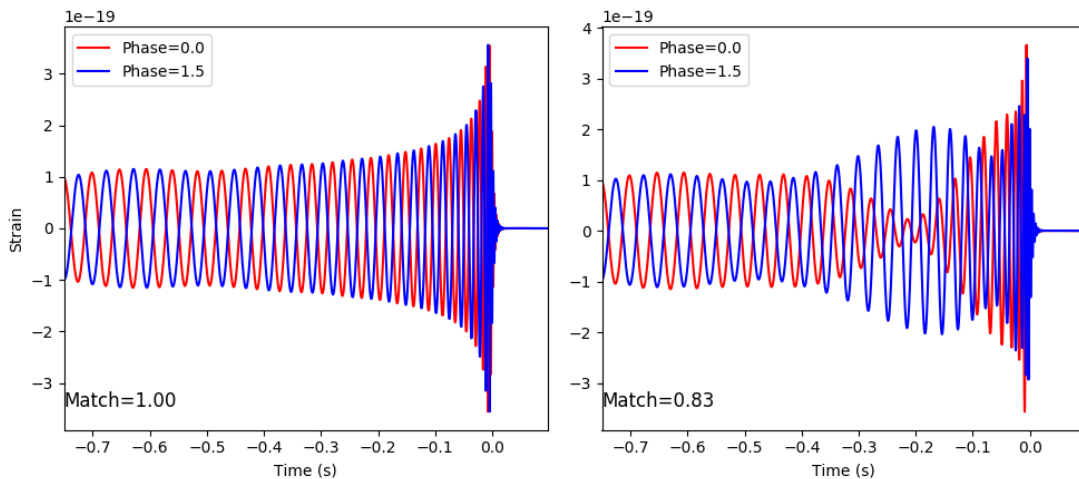


Figure 9: Affect of phase on non-precessing and precessing waveforms. Precession adds an extra degree of freedom in that the morphology of precessing waveforms is different for different phases.

have a stronger signal, there is less opportunity for precessive effects to manifest.

## 2.2 Matching and exploring the parameter space

An extremely useful and computationally cheap way to identify some of these degeneracies is through the process of matching as defined in (13). In the *PyCBC* framework, the match is maximised over extrinsic parameters such as distance and source location that only affect the amplitude of a signal, and so is a useful tool for examining the similarities in the morphologies of different waveforms. A match takes values in the range  $[0, 1]$ , with identical waveforms having a match of 1. It is also important to note that the inclination parameter has a similar nature of that of the initial phase, in that in matches of non-precessing binaries it can be maximised over as it does not affect signal morphology, however once precession is added, waveforms at different inclinations no longer match, further adding to the complexity of the parameter space.

In this section we intend to get some idea of the areas in which we expect the detector to be most sensitive to precession, and those in which precessing signals are intrinsically degenerate with non-precessing waveforms. This is done by finding the match between waveforms with and without in-plane spin for a range of parameters. In the case of a strong match ( $> 0.95$ ), it is unlikely that  $\chi_p$  can be accurately and precisely recovered for signals with those parameters due to an intrinsic similarity of the waveforms.

Fig. 10 shows how the matches between precessing and non-precessing waveforms change with inclination for four different mass ratios. The dark regions of the match is where the signals have significant mismatch, and the waveforms should be well distinguished, and the light regions are where the waveforms are effectively degenerate. It is apparent that the degeneracy is far stronger for close to equal mass binaries, where only maximally precessing systems at edge-on inclinations will have noticeably different waveforms. Here we plot the 0.97 match contour as it is generally expected that the advanced LIGO detectors should be able to distinguish between waveforms with a match of 0.97.

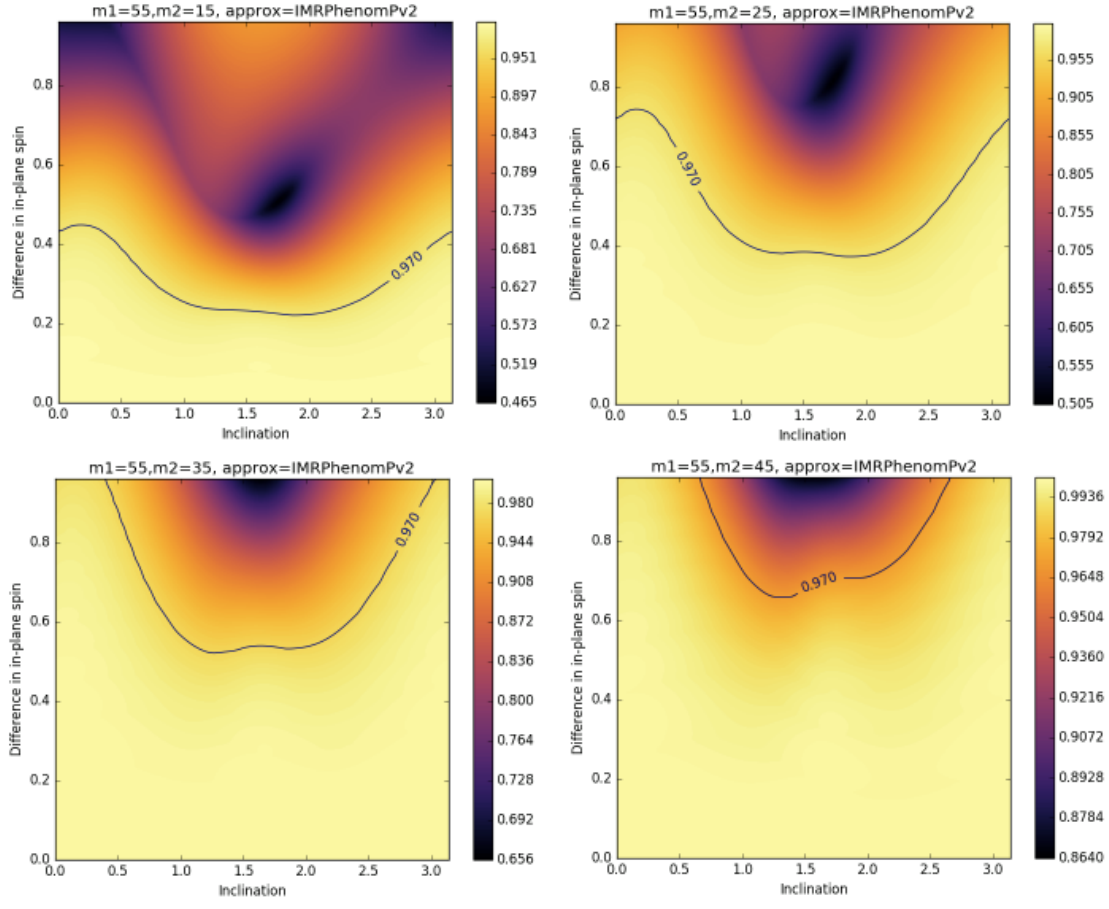


Figure 10: Matches between precessing and non-precessing waveforms for a range of inclinations and mass ratios.(make this more compact before submit)

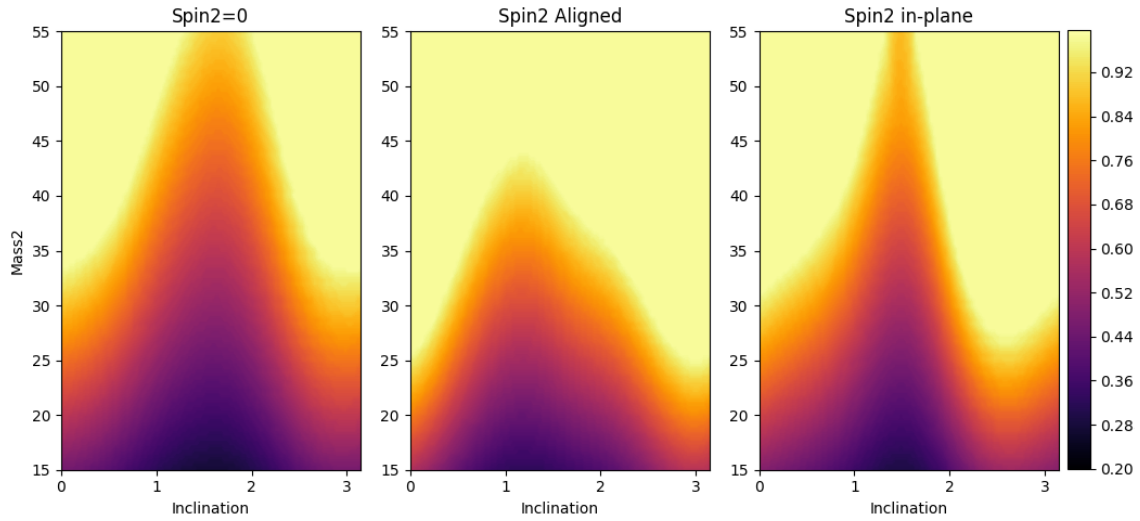


Figure 11: Spin difference required for the match between precessing and non-precessing waveforms to drop below 0.95



For all but the most extreme mass ratios, a combination of significant in-plane spin ( $\geq 0.6$ ) and/or strong inclination is necessary to have any significant deviation for systems with high precession. It is important to remember here that as we change the inclination, the overall strength of the signal will drop as the amplitude of the gravitational wave is lower (with the peak at  $\iota = 0$ ), and the matching process does not account for this change in signal strength.

In Fig. 11, we examine the effect of the spin on the lower mass black hole on matches between precessing and non-precessing waveforms. In these figures, for a ranges of inclinations and mass ratios, we find the minimum spin difference required for the match between waveforms to drop below 0.95. This is an efficient way of quantifying the precessing degeneracy for a range of parameters. The dark regions are areas where only a small difference in spin is required for the match to drop, and the light areas show where the waveforms are degenerate. In Fig. 11 we compare results for systems with no spin, spin aligned with  $\vec{L}$  and fully in-plane spin on the smaller black hole. The spin on the smaller black hole appears to only have a significant effect the matches around an inclination of 1.5, where the system is edge on, but other than that it does not drastically change the structure of the parameter space. This is convenient as it indicates that inference results for systems with  $|\vec{S}_2| = 0$  should be broadly applicable to those with arbitrary spins on the smaller black hole. It is also evident that the mass ratio does not appear to affect the shape of the parameter space, but more the intensity with which the match changes as a function of inclination. So we can expect the same behaviour at different mass ratios, just with the degeneracies being weaker or higher for extreme and close mass ratios respectively.

Lastly we explore the impact of polarisation and phase on the parameter space, using the same technique as in Fig. 11. We select an extreme mass ratio binary here ( $m_1 = 55, m_2 = 15$ ) to highlight any prominent features of the parameter space. A full range of inclinations and phases are shown for four polarisations: plus, mixed but plus dominated, mixed but cross dominated, and cross polarisations. The region of extremely high sensitivity at  $\iota = \pi/2$  is a result of the fact that there is no cross-polarised signal for an edge-on binary. The parameter space appears to be highly structured, and dependent on both phase and inclination. The effect of polarisation appears to be strongest around  $\pi/2$ , and does not have such a large impact at other inclinations or phases.

### 3 Detector response simulations

In this section we describe the process of inserting signals into simulated detector noise, and then perform a full parameter estimation.

#### 3.1 Signal extraction

Data whitening - basically LOSC stuff, how we go from raw data to a signal - move this to intro?

#### 3.2 Inference pipeline

A large number of software injections were going to be necessary to generate any interesting results due to the large size and complexity of the parameter space as revealed by the match results. So it was key that they could be performed efficiently and in an organised

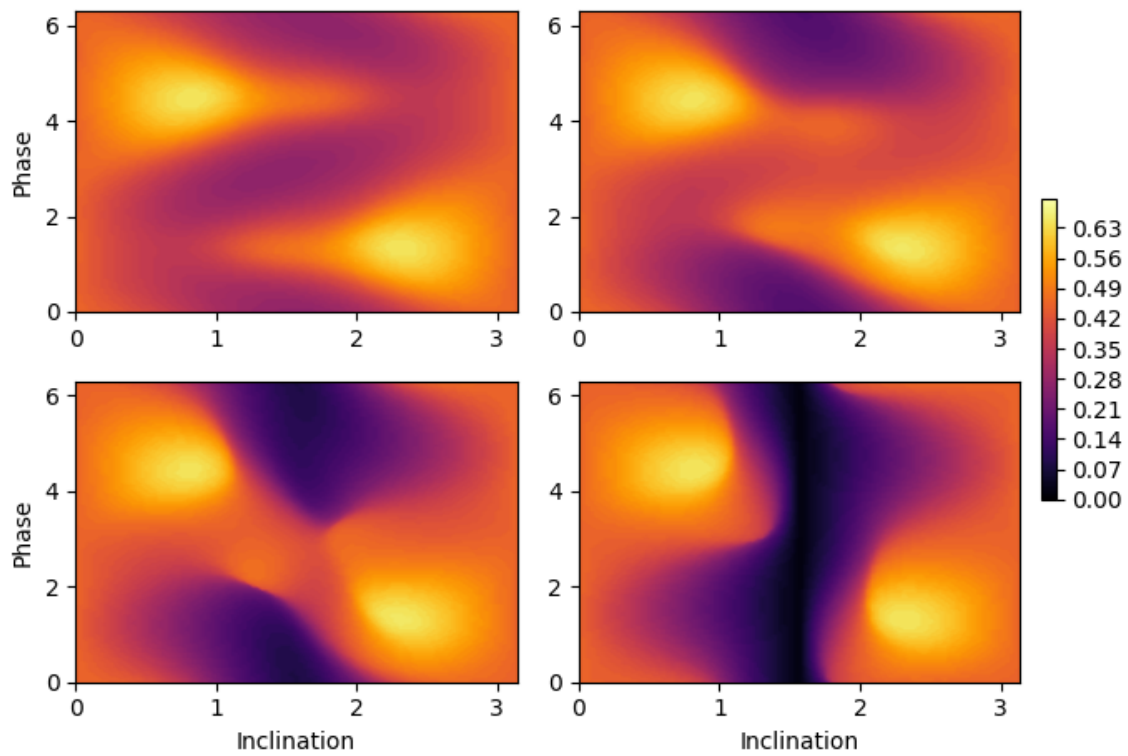


Figure 12: Match limit plots for a range of inclinations and phases for 4 polarisations.

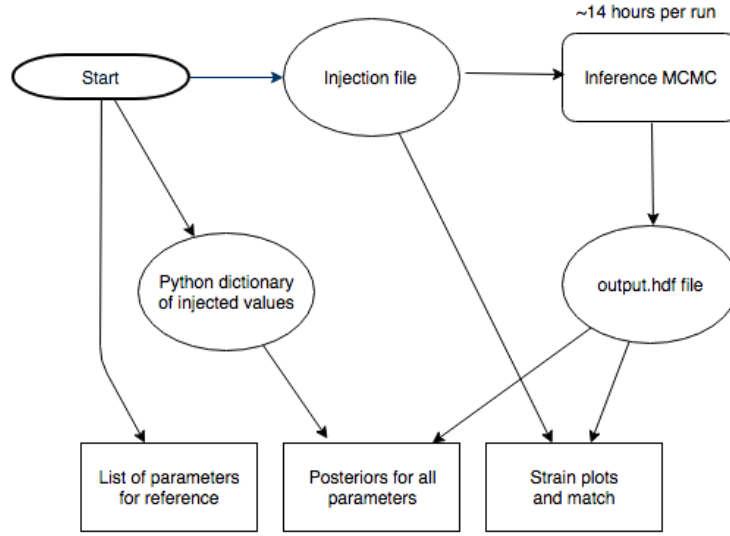


Figure 13: Flow chart of the inference pipeline. The ellipses represent data files that were generated during the pipeline and stored in case further analysis was necessary. The boxes at the bottom represent the final output of the pipeline.

way. This required the construction of an inference pipeline which formed the bulk of the computational work of the project. This was ultimately one bash script that would create a new folder for each run, generate the injection file and run the inference MCMC. It also saves the injected parameters as a python dictionary, plots all posteriors overlaid with injected parameters, plots the injected waveform, and the recovered (maximum posterior, or *MAP* waveform) and injected waveforms overlaid on the whitened detector strain data, and return matches between the MAP and injected waveforms. This meant that all the relevant analysis and data processing needed for each inference run was fully automated. A flow chart of this process is shown in Fig. 12. For the MCMC parameters, in order to achieve a balance between computation time and result accuracy, 5,000 samplers were used and 12,000 iterations, and the burn-in process was skipped. These parameters were kept the same for all software injections. This project work was also split between a number of different LIGO clusters, as well as work on several different local PCs, and so the pipeline along with all the relevant match and precession scripts were maintained as part of a GitHub repository which meant that the codes could be developed effectively and without conflict.

### 3.3 Inference results

In this section we present the results from a range of inference runs, attempt to assess the effectiveness of spin estimation and compare the inference results with the match results to evaluate how effective the match process is as a predictor of inference accuracy. For all injections we set  $S_{1\perp} = 0.9$  and  $|\vec{S}_2| = 0$  with  $\chi_p = 0.9$ , and cover a uniform range of inclinations. We set the phase to be  $\phi = 0.$ , and the polarisation angle  $\psi = 0.8$ , so the signals are of mixed polarisation, but slightly cross dominated. The match results indicate that cross polarised signals generally have a higher spin resolution, but we want to

avoid the signal drop at  $\iota = \pi/2$ , which is why a mixed but cross dominated polarisation angle was selected. The source location and coalescence time were also kept fixed for all injections. We also only examine high mass ratio binaries, as the match results indicate that precession is not significant in equal mass ratio binaries. Prior distributions are all uniform, with mass ranging  $[5, 80]$  and distance in the range  $[100, 1000]$ , and sky location and spin orientations all have isotropic priors. Out of a total of \*\*\*\*\* software injections that were performed, there were only \*\*\*\* instances where the injected  $\chi_p$  value fell within the 90% confidence interval. In Figs 14 and 15 we compare posteriors for two inferences, where  $\chi_p$  was excluded and where it was recovered moderately well, and we refer to these as A and B respectively. Even in the cases where the injected value was within the 90% confidence intervals, it was always closer to the upper bound than to the mean, and a mean  $\chi_p$  greater than 0.65 was never found.

Neither sets of posteriors are consistently accurate, although overall the results of injection A are overall significantly more accurate than those for B, with the exceptions of  $\chi_p$  and  $\iota$ . The masses and source locations are recovered well, with the injected value lying within the 90% confidence intervals. However the 'cost' of recovering  $\chi_p$  seems to be having significant inaccuracies on a range of important parameters, with  $\chi_{eff}$ ,  $m2$ , distance and chirp mass all being excluded. To examine the source of this inaccuracy, in Fig 16 we plot the whitened detector strain with the signal embedded into it, overlaid with the MAP waveform as recovered by the inference process, and the injected waveform. A match is also performed between the MAP and injected waveforms in each detector frame. This is a crucial part of the analysis, as it helps to distinguish between different sources of inaccuracy. If the inaccuracies are due to either detector noise or some error in the MCMC process, we should expect a low match between the MAP and injected waveform. However it is also possible that due to the large number of parameters, the MCMC algorithm has found certain combinations of different parameters that lead to an effectively degenerate waveform. In this case, we would expect a high match between the MAP waveform and injected waveform, despite the fact that they have vastly different parameters.

The results shown in Fig. 16 show a stronger match for A, where the majority of parameters were more accurately recovered. In particular, for B, L1 shows a low match of 0.93 between MAP and injected waveforms. This is likely due to the precessive effects which are most apparent around  $-0.4s$ , where the injected signal is almost entirely flat, and later on during the inspiral around  $-0.2s$  where there is notable disagreement between the signals. In this case, it is clear that the inference process has not found an optimal template waveform to replicate the injected signal. However in the case of A there is a strong match between waveforms, and it is clear from the strain plot that the MAP waveform matches the strain data extremely well. There is, however, a mild disagreement during the late merger and ringdown, which is the source of the mismatches of 0.01 and 0.02. Since the match is so strong, the waveforms themselves must be intrinsically degenerate up to deviation that occurs at the merger.

If two signals are degenerate for the majority of the inspiral and merger, and only during the end of the merger and ringdown do they differ, it will be extremely difficult for LIGO detectors to differentiate between them, as the very short time period where there is any mismatch will be swamped by noise. Returning to Fig. 14, we can see that even though the match is strong, there are significant inaccuracies on  $\chi_p$  and  $\iota$ . So in A and B we have examples of each inaccuracy as described earlier - one down to poor signal recovery and one down to an intrinsic degeneracy. In Figs 17 and 18, results are shown for case C,

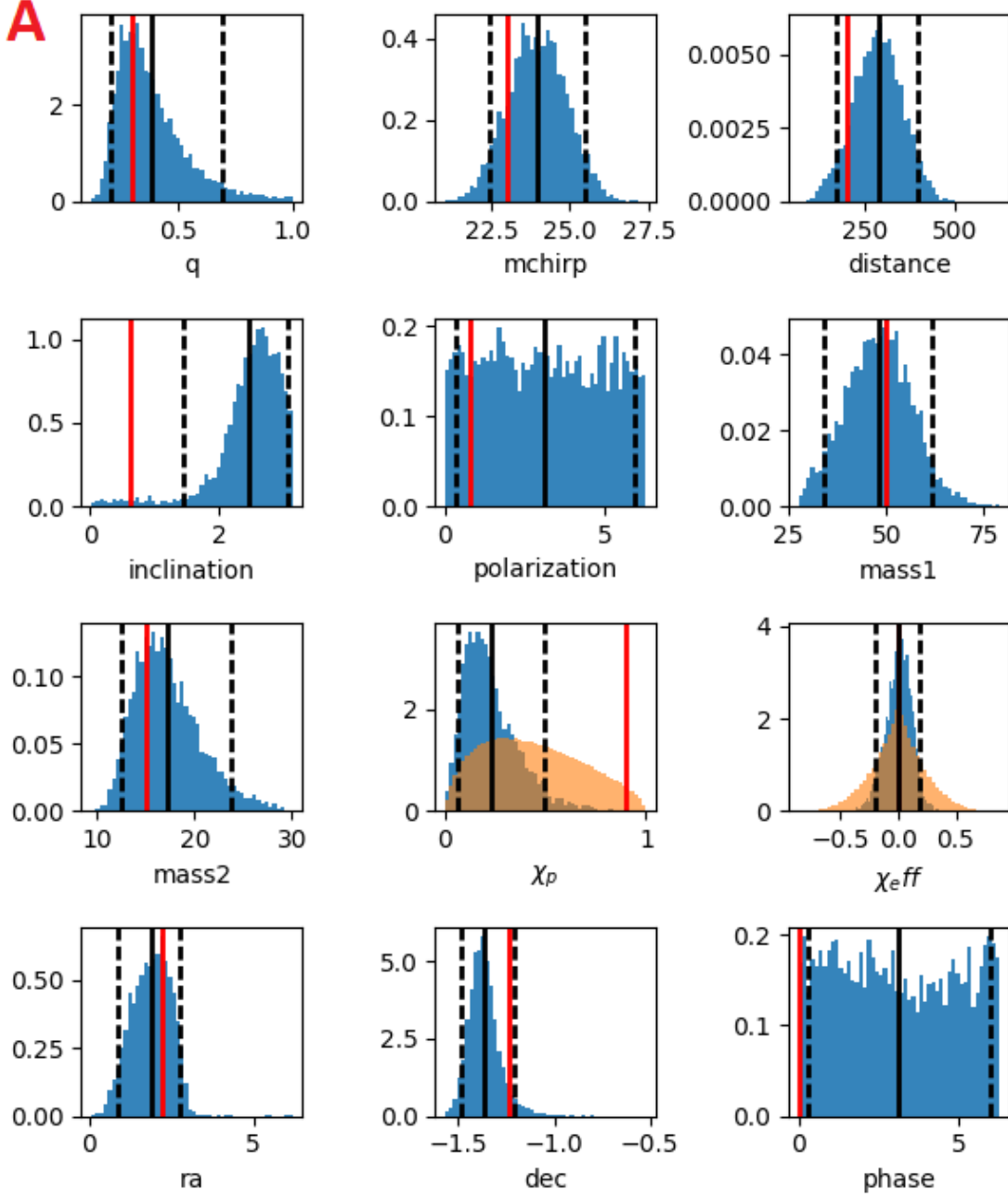


Figure 14: Posteriors for an injection with  $m_1 = 50$ ,  $m_2 = 15$ ,  $\iota = 2.51$ ,  $\phi = 0$ ,  $\psi = 0.8$  at a distance of 200Mpc. Prior distributions are included for the derived spin parameters  $\chi_p$  and  $\chi_{eff}$ , which result from uniform spin magnitude and isotropic orientation distributions. The red bar shows the injected value, with the black solid line showing the mean of the posterior, and the black dashed line showing the 90% confidence intervals, which are the standard error margins quoted on LIGO inference results.

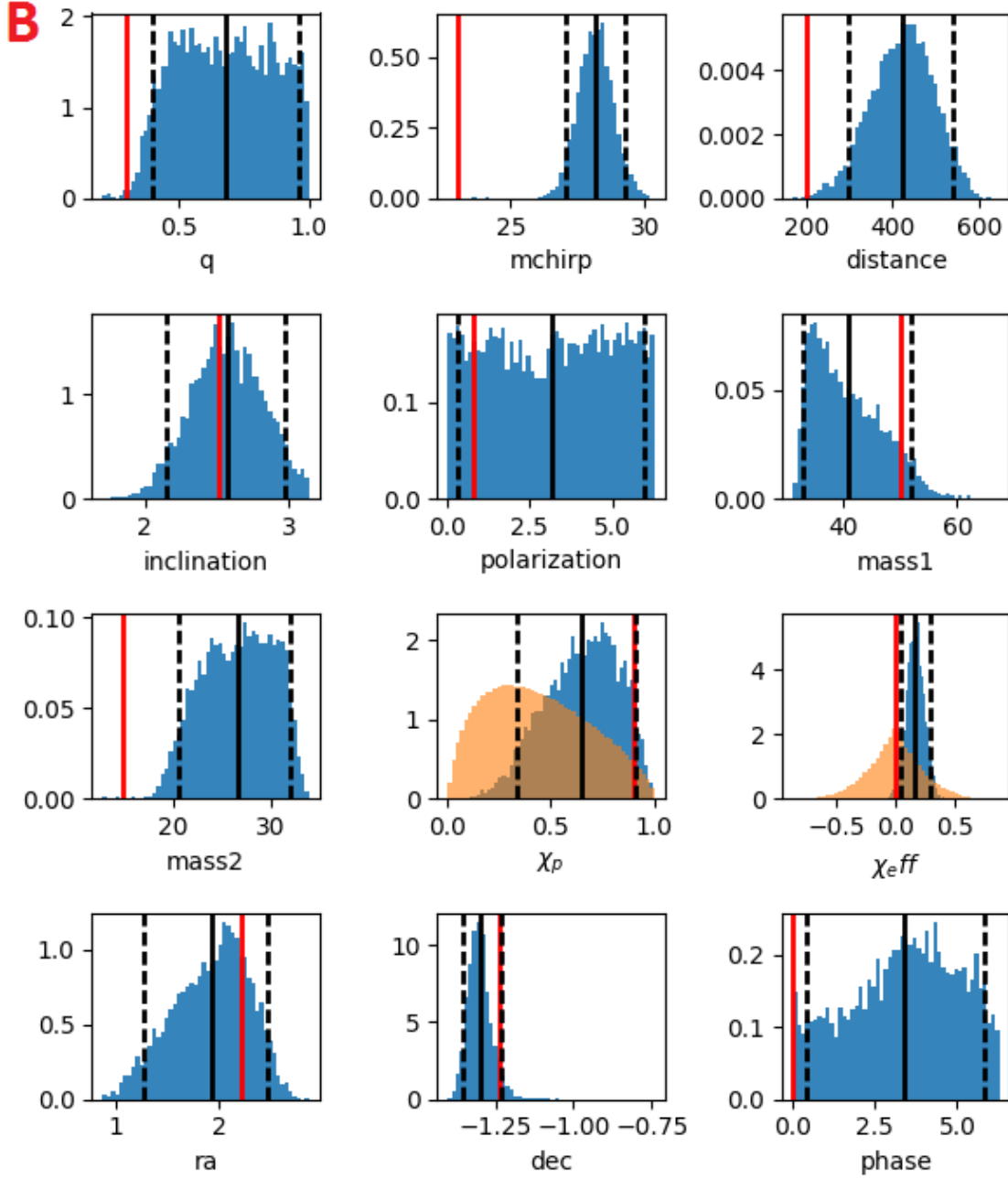


Figure 15: Posteriors for an injection with the same parameters as in Fig. 14, except here with an inclination of  $\iota = 0.63$

which was selected as its waveform had the strongest visible precessive effects in both H1 and L1 detector frames.

From Fig. 18 it can be seen that the amplitude of the signal noticeably drops towards the end of the inspiral and just before the merger, implying that this would be an ideal signal to recover a high value of  $\chi_p$  from. The posteriors shown in Fig. 17 are mostly accurate, with the majority of injected parameters lying inside the 90% confidence intervals, however once again  $\chi_p$  is excluded, and significantly underestimated. The match values shown in Fig. 18 are strong, with both detectors giving a match of 0.96 between the injected and MAP waveforms. This is further evidence of an intrinsic degeneracy that prevents high  $\chi_p$  MAP values from being found. For all posteriors shown, both  $\phi$  and  $\psi$  are broadly uniform, and in the case where they are not uniform, they are largely inaccurate. However in section 2 it was observed that  $\psi$  and especially  $\phi$  have a significant effect on the structure of the parameter space, and the match between precessing and non-precessing waveforms.

One possible explanation for this uniformity is that for each stochastically selected phase and polarisation, the MCMC algorithm readily finds a good match between the injected signal and the strain data simply by tweaking the other remaining parameters slightly. If this is the case, since there are a larger number of waveforms in the template bank with lower values of  $\chi_p$  (as shown in the prior distributions), if these waveforms can still match the signal well just by slightly changing inclination, source location and masses, we would expect the MCMC algorithm to favour lower values of  $\chi_p$  but with slightly larger uncertainties on the other posteriors. This explanation is exemplified by the waveforms in Fig. 8, where it is shown that the magnitude of the precessive effect is not necessarily proportional to  $\chi_p$ . It is also interesting to note that  $\chi_{eff}$  parameters are generally relatively accurate, which implies it is mainly spin magnitude that is being underestimated, but the orientations are recovered accurately.

### 3.4 Inclination and precession

Next we examine the effect of inclination on  $\chi_p$  recovery. Software injections were performed for a range of inclinations at two distances, 200Mpc and 800Mpc, which simulate a strong and weak signal respectively. Posteriors for  $\chi_p$  and  $\chi_{eff}$  are shown in Fig. 19 for 6 inclinations in the range  $[0, \pi]$ , with the injected values shown by the red bar. Interestingly there is no apparent correlation between the trends for  $\chi_p$  at 200Mpc and at 800Mpc. If anything the trends appear to be opposite, with the most greater accuracy at face-on for the signals at 200Mpc, and greatest accuracy close to edge-on for the 800Mpc signals. As in the previous results,  $\chi_{eff}$  is recovered consistently well with the exception of two results around  $\iota \approx 2$  in the 200Mpc signals, again implying that spin orientation is accurate, but magnitude is underestimated. Therefore there appears to be no clear correlation between  $\chi_p$  and  $\chi_{eff}$  accuracy.

In Fig. 20 we attempt to identify how well the posteriors in Fig. 19 correlate with the predicted trends from the match results in Figs. 10 and 11. If the match process were a reliable method of predicting inference results, the posteriors for  $\chi_p$  around inclinations of 1 to 2 should be the most accurate, as precessing waveforms are most distinct from non-precessing ones here. However the 200Mpc results in fact show the opposite trend, and accuracy drops to a minimum around this area.

### 3.5 Impact of Virgo

A look at how Virgo will influence PE, especially chi p estimation.

## 4 Conclusions

Summary of results on PE and estimation of chi p, and a prospect on Virgo's impact.

## 5 Reflective Statement

I now need a therapist

Still to do:

6. Conclusions 7. Proper references of pics

## References

- [1] B. P. Abbott et. al. Observation of gravitational waves from a binary black hole merger. *Physical Review Letters*, 116(6), Feb 2016.
- [2] B. P. Abbott et. al. GW151226: Observation of gravitational waves from a 22-solar-mass binary black hole coalescence. *Physical Review Letters*, 116(24), Jun 2016.
- [3] A. Einstein. Nherungsweise integration der feldgleichungen der gravitation. *Sitzungsberichte der Kniglich Preussischen Akademie der Wissenschaften Berlin*, (688-696), 1916.
- [4] A. Einstein. ber gravitationswellen. *Sitzungsberichte der Kniglich Preussischen Akademie der Wissenschaften Berlin*, (154-167), 1918.
- [5] W. Steinicke. Einstein and the gravitational waves. *Astronomische Nachrichten*, 326(7), 2005.
- [6] N. Rosen A. Einstein. On gravitational waves. *Journal of the Franklin Institute*, 223(43-54), 1937.
- [7] J. H. Taylor and J. M. Weisberg. A new test of general relativity - gravitational radiation and the binary pulsar PSR 191316. *The Astrophysical Journal*, 253:908, Feb 1982.
- [8] Marica Branchesi. Multi-messenger astronomy: gravitational waves, neutrinos, photons, and cosmic rays. *Journal of Physics: Conference Series*, 718:022004, May 2016.
- [9] B. P. Abbott et. al. Prospects for observing and localizing gravitational-wave transients with advanced ligo and advanced virgo. *Living Reviews in Relativity*, 1:19, Dec 2016.
- [10] B. P. Abbott et al. Tests of general relativity with GW150914. *Physical Review Letters*, 116(22), May 2016.
- [11] Nicolás Yunes, Kent Yagi, and Frans Pretorius. Theoretical physics implications of the binary black-hole mergers GW150914 and GW151226. *Physical Review D*, 94(8), Oct 2016.



- [12] Xavier Calmet, Iberê Kuntz, and Sonali Mohapatra. Gravitational waves in effective quantum gravity. *The European Physical Journal C*, 76(8), Jul 2016.
- [13] Pau Amaro-Seoane et al. Low-frequency gravitational-wave science with eLISA/NGO. *Classical and Quantum Gravity*, 29(12):124016, Jun 2012.
- [14] Alex Nitz, Ian Harry, Christopher M. Biwer, Duncan Brown, Josh Willis, Tito Dal Canton, Larne Pekowsky, Thomas Dent, Andrew R. Williamson, Collin Capano, Soumi De, Bernd Machenschalk, Prayush Kumar, Miriam Cabero, Thomas Massinger, Amber Lenon, Stephen Fairhurst, Steven Reyes, Alex Nielsen, shasvath, Francesco Pannarale, Leo Singer, Stanislav Babak, Duncan Macleod, CBC Sugar, Lorena Magaia Zertuche, John Veitch, couvares, Brian Bockelman, and nwbrown. ligo-cbc/pycbc: O2 production release 11, April 2017.
- [15] James B. Hartle. *Gravity: An Introduction to Einstein's General Relativity*. Addison Wesley, 2003.
- [16] Unknown. Accessed 09/04/2017.
- [17] Luc Blanchet, Thibault Damour, Bala R. Iyer, Clifford M. Will, and Alan G. Wiseman. Gravitational-radiation damping of compact binary systems to second post-newtonian order. *Physical Review Letters*, 74(18):3515–3518, May 1995.
- [18] Swinburne Astronomy Productions. Accessed 09/04/2017.
- [19] Advanced ligo fig. [https://upload.wikimedia.org/wikipedia/commons/d/d5/Simplified\\_diagram\\_of\\_an\\_Advanced\\_LIGO\\_detector.png](https://upload.wikimedia.org/wikipedia/commons/d/d5/Simplified_diagram_of_an_Advanced_LIGO_detector.png), 10/04/2017.
- [20] Rana X. Adhikari. Gravitational radiation detection with laser interferometry. *Reviews of Modern Physics*, 86(1):121–151, Feb 2014.
- [21] D. V. Martynov et al. Sensitivity of the advanced LIGO detectors at the beginning of gravitational wave astronomy. *Physical Review D*, 93(11), Jun 2016.
- [22] J. et al. Abadie. Sensitivity Achieved by the LIGO and Virgo Gravitational Wave Detectors during LIGO's Sixth and Virgo's Second and Third Science Runs. 2012.
- [23] J Aasi et al. Advanced LIGO. *Classical and Quantum Gravity*, 32(7):074001, Mar 2015.
- [24] D. V. et al. Martynov. Sensitivity of the advanced ligo detectors at the beginning of gravitational wave astronomy. *Phys. Rev. D*, 93:112004, Jun 2016.
- [25] Robert L. Forward. Wideband laser-interferometer gravitational-radiation experiment. *Phys. Rev. D*, 17:379–390, Jan 1978.
- [26] C. Capano, I. Harry, S. Privitera, and A. Buonanno. Implementing a search for gravitational waves from non-precessing, spinning binary black holes. *ArXiv e-prints*, February 2016.
- [27] B. P. et al. Abbott. Gw150914: First results from the search for binary black hole coalescence with advanced ligo. *Phys. Rev. D*, 93:122003, Jun 2016.

- [28] B. P. Abbott et al. Properties of the binary black hole merger GW150914. *Physical Review Letters*, 116(24), Jun 2016.
- [29] Emily Baird, Stephen Fairhurst, Mark Hannam, and Patricia Murphy. Degeneracy between mass and spin in black-hole-binary waveforms. *Physical Review D*, 87(2), Jan 2013.
- [30] Curt Cutler and Éanna E. Flanagan. Gravitational waves from merging compact binaries: How accurately can one extract the binary’s parameters from the inspiral waveform? *Phys. Rev. D*, 49:2658–2697, Mar 1994.
- [31] J. Veitch et al. Parameter estimation for compact binaries with ground-based gravitational-wave observations using the LALInference software library. *Physical Review D*, 91(4), Feb 2015.
- [32] M. V. van der Sluys, C. Rver, A. Stroeer, V. Raymond, I. Mandel, N. Christensen, V. Kalogera, R. Meyer, and A.M Vecchio. Gravitational-wave astronomy with inspiral signals of spinning compact-object binaries. *The Astrophysical Journal Letters*, 688(2):L61, 2008.
- [33] J. et al. Aasi. Parameter estimation for compact binary coalescence signals with the first generation gravitational-wave detector network. *Phys. Rev. D*, 88:062001, Sep 2013.
- [34] Archisman Ghosh, Walter Del Pozzo, and Parameswaran Ajith. Estimating parameters of binary black holes from gravitational-wave observations of their inspiral, merger, and ringdown. *Phys. Rev. D*, 94:104070, Nov 2016.
- [35] Alessandra Buonanno, Yanbei Chen, Yi Pan, and Michele Vallisneri. Quasiphysical family of gravity-wave templates for precessing binaries of spinning compact objects: Application to double-spin precessing binaries. *Physical Review D*, 70(10), Nov 2004.
- [36] P. Ajith, M. Hannam, S. Husa, Y. Chen, B. Brügmann, N. Dorband, D. Müller, F. Ohme, D. Pollney, C. Reisswig, L. Santamaría, and J. Seiler. Inspiral-merger-ringdown waveforms for black-hole binaries with nonprecessing spins. *Phys. Rev. Lett.*, 106:241101, Jun 2011.
- [37] Carl L. Rodriguez, Benjamin Farr, Vivien Raymond, Will M. Farr, Tyson B. Littenberg, Diego Fazi, and Vicky Kalogera. BASIC PARAMETER ESTIMATION OF BINARY NEUTRON STAR SYSTEMS BY THE ADVANCED LIGO/VIRGO NETWORK. *The Astrophysical Journal*, 784(2):119, Mar 2014.
- [38] M. V. van der Sluys, C. Rver, A. Stroeer, V. Raymond, I. Mandel, N. Christensen, V. Kalogera, R. Meyer, and A. M Vecchio. Gravitational-wave astronomy with inspiral signals of spinning compact-object binaries. *The Astrophysical Journal Letters*, 688(2):L61, 2008.
- [39] Salvatore Vitale, Ryan Lynch, Vivien Raymond, Riccardo Sturani, John Veitch, and Philip Graff. Parameter estimation for heavy binary-black holes with networks of second-generation gravitational-wave detectors. *Physical Review D*, 95(6), mar 2017.

- [40] Theodoros A. Apostolatos, Curt Cutler, Gerald J. Sussman, and Kip S. Thorne. Spin-induced orbital precession and its modulation of the gravitational waveforms from merging binaries. *Phys. Rev. D*, 49:6274–6297, Jun 1994.
- [41] Lawrence E. Kidder. Coalescing binary systems of compact objects to (post)<sup>5/2</sup>-newtonian order. v. spin effects. *Phys. Rev. D*, 52:821–847, Jul 1995.
- [42] Patricia Schmidt, Frank Ohme, and Mark Hannam. Towards models of gravitational waveforms from generic binaries: II. modelling precession effects with a single effective precession parameter. *Phys. Rev. D*, 91:024043, Jan 2015.
- [43] Salvatore Vitale, Ryan Lynch, John Veitch, Vivien Raymond, and Riccardo Sturani. Measuring the spin of black holes in binary systems using gravitational waves. *Physical Review Letters*, 112(25), Jun 2014.
- [44] Andrea Taracchini, Alessandra Buonanno, Yi Pan, Tanja Hinderer, Michael Boyle, Daniel A. Hemberger, Lawrence E. Kidder, Geoffrey Lovelace, Abdul H. Mroué, Harald P. Pfeiffer, Mark A. Scheel, Béla Szilágyi, Nicholas W. Taylor, and Anil Zenginoglu. Effective-one-body model for black-hole binaries with generic mass ratios and spins. *Phys. Rev. D*, 89:061502, Mar 2014.
- [45] B. P. Abbott et al. Astrophysical implications of the binary black-hole merger gw150914. *The Astrophysical Journal Letters*, 818(2):L22, 2016.

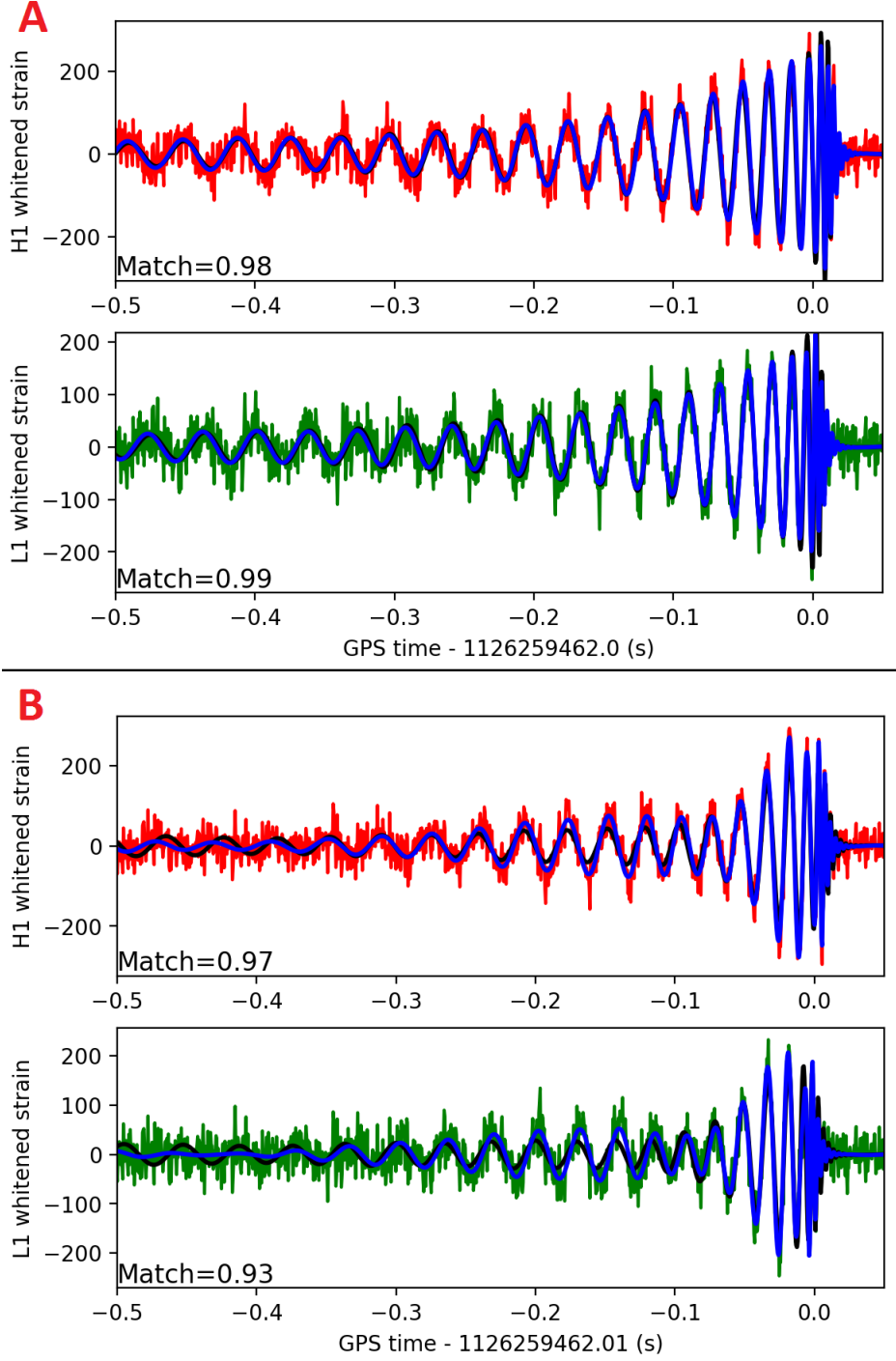


Figure 16: Strain plots for both H1 and L1 detectors. The top two graphs show the strain data corresponding to the results in Fig. 14, the bottom two graphs correspond to Fig. 15. The green and red lines show the whitened strain data, the black line is the MAP waveform and the injected waveform is shown in blue.

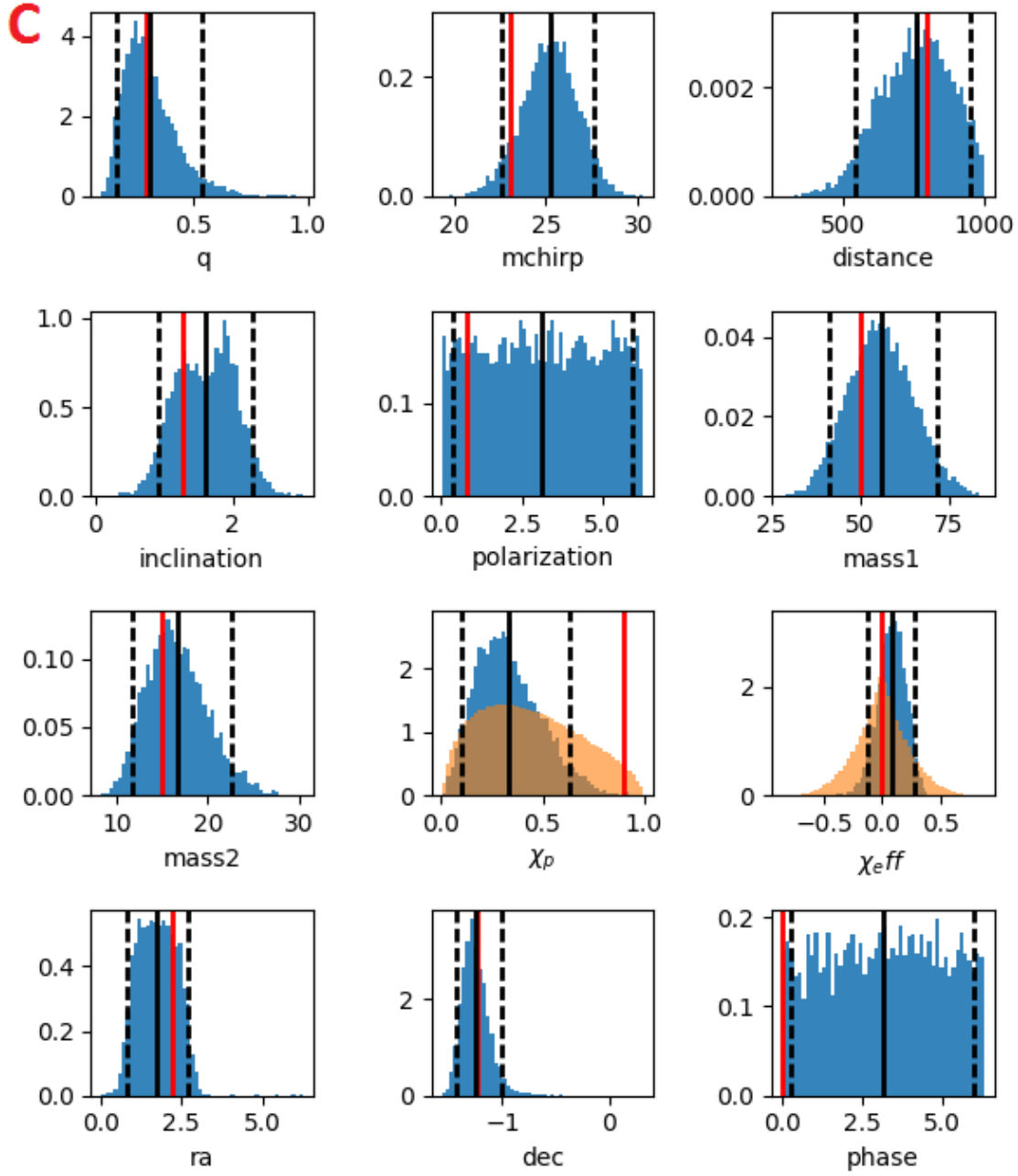


Figure 17: Posteriors for injection C, which has the same parameters as in Fig. 14, but with an inclination of  $\iota = 1.26$  and at a distance of 800Mpc.

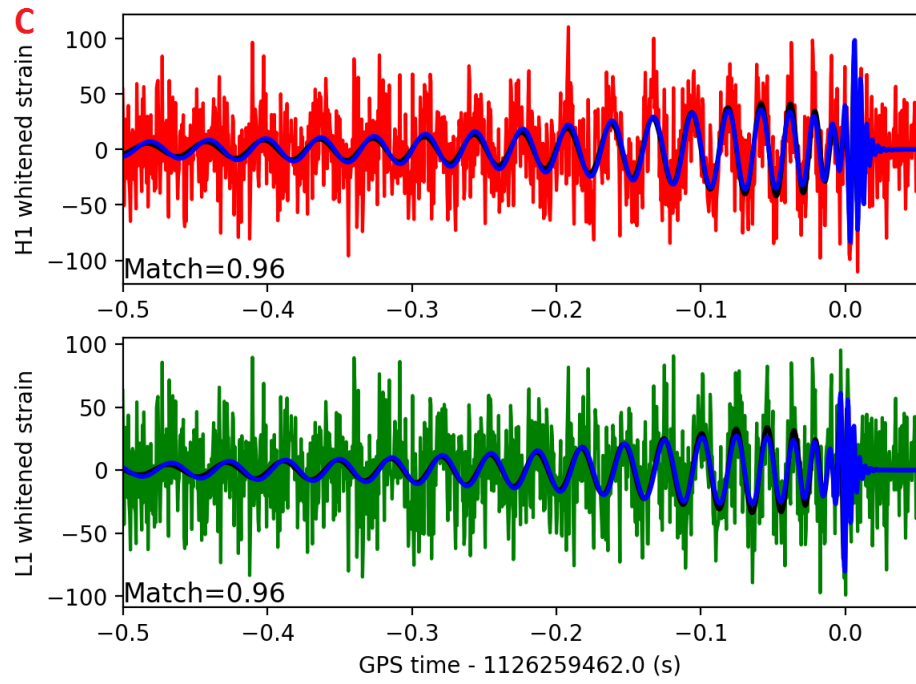


Figure 18: Strain plot of injection C, a waveform with strong precessive modulation.

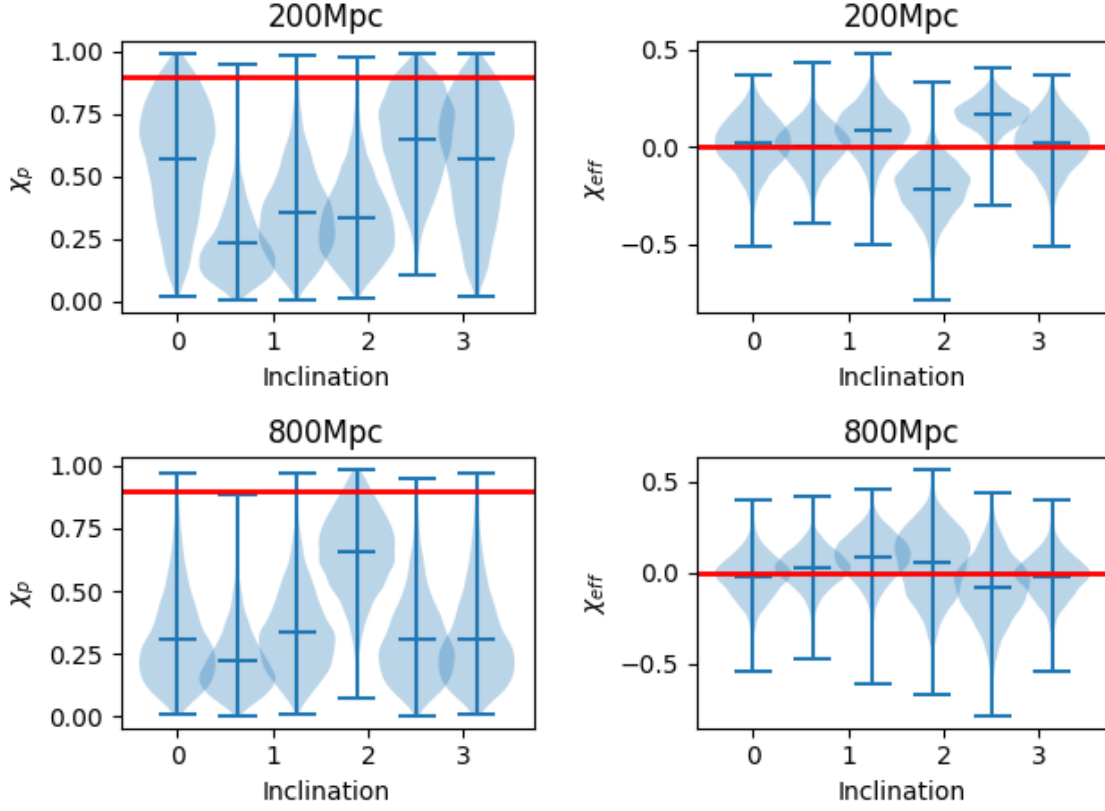


Figure 19: Comparisons of derived spin parameters as a function inclination for strong and weak signals. All other parameters are kept the same as listed in Fig. 14.

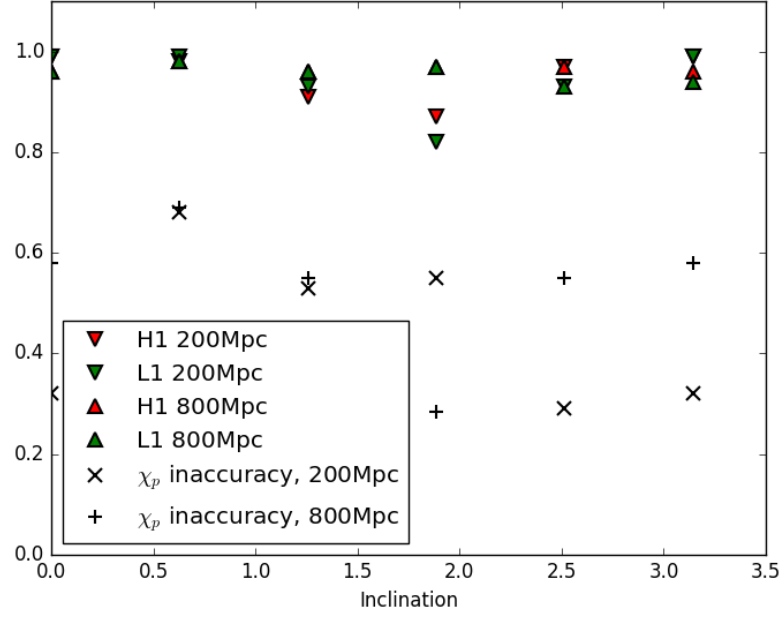


Figure 20: Match between MAP and injected waveforms along with spin inaccuracy for the 200Mpc and 800Mpc runs as a function of inclination.

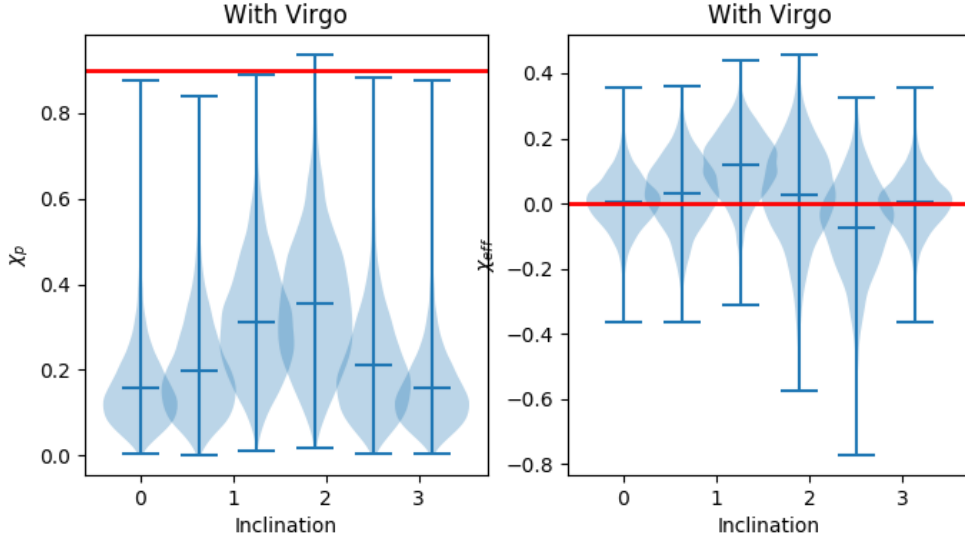


Figure 21: Plots showing  $\chi_p$  and  $\chi_{eff}$  for a range of inclinations at 200Mpc with the VIRGO detector included in the inference process.